

Numerical Simulation of a Nanosecond Pulse Discharge in Mach 5 Flow

Jonathan Poggie* and Nicholas J. Bisek†

Air Force Research Laboratory, Wright-Patterson AFB, Ohio 45433-7512 USA

Igor V. Adamovich‡ and Munetake Nishihara§

The Ohio State University, Columbus, Ohio 43210 USA

A physics-based model was developed for nanosecond-pulse discharges, including realistic air kinetics, electron energy transport, and compressible bulk gas flow. A reduced plasma kinetic model (23 species and 50 processes) was developed to capture the dominant species and reactions for energy storage and thermalization in the discharge. The kinetic model included electronically and vibrationally excited species, and several species of ions and ground state neutrals. The governing equations included the Poisson equation for the electric potential, diffusion equations for each neutral species, conservation equations for each charged species, and mass-averaged conservation equations for the bulk gas flow. The results of calculations with this model highlighted the path of energy transfer in the discharge. At breakdown, the input electrical energy was transformed over a timescale on the order of 1 ns into chemical energy of ions, dissociation products, and vibrationally and electronically excited particles. About 30% of this energy was subsequently thermalized over a timescale of 10 μ s. Since the thermalization time scale was faster than the acoustic time scale, the heat release led to the formation of weak shock waves originating near the sheath edge, consistent with experimental observations.

I. Introduction

In a nanosecond-pulse discharge, the input energy in the electrical circuit is ultimately converted into heat and gas motion. Motivated by potential uses in flow control applications, we are interested in the details of the physics of this process.

Repetitive, pulsed discharges are a well-known and appealing method for plasma generation.^{1–3} Such discharges are efficient generators of both ions and electronically excited species because of their high instantaneous reduced electric field.⁴ In aerospace applications, nanosecond-pulse discharges have been employed as flow control actuators,^{5–8} as a source of ionization for nonequilibrium magnetohydrodynamic devices,^{9,10} and as a means for enhancing ignition and combustion.^{11,12}

The generation of shock waves by volumetric heat release in pulsed discharges was observed and explained in the 1970s in the context of gas laser technology.^{13,14} Early computations by Aleksandrov et al.¹⁴ assumed that all the power dissipated in the discharge immediately went into heating the neutral gas. Popov,¹⁵ however, has proposed a two-stage heating mechanism in which product species and electronically excited species are generated by electron impact, and then the stored chemical energy is converted to thermal energy through quenching and recombination reactions. (Reports on other investigations of kinetic mechanisms can be found in Refs. 16–18.) Two-dimensional calculations have been carried out recently by Unfer and Boeuf,¹⁹ assuming instant thermalization of 30% of the dissipated power that goes into electronic excitation.

In recent experiments by Nishihara et al.,²⁰ control of a Mach 5 cylinder flow was demonstrated using a pulsed surface dielectric barrier discharge. The hollow cylinder model was made of fused quartz. A thin

*Senior Aerospace Engineer, Hypersonic Sciences Branch. Associate Fellow AIAA.

†Research Aerospace Engineer, Hypersonic Sciences Branch. Member AIAA.

‡Professor, Department of Mechanical Engineering. Associate Fellow AIAA.

§Postdoctoral Researcher, Department of Mechanical Engineering. Member AIAA.

copper exposed electrode was affixed to the surface of the cylinder, with a second copper electrode mounted inside. A combination of positive and negative polarity pulses applied to the two electrodes produced a potential difference of about 27 kV, lasting on the order of 5 ns (pulse full-width at half maximum). The effects of the energy release in the resulting discharge were captured using phase-locked schlieren imaging. A weak shock wave was seen to form near the edge of the exposed electrode, and propagate upstream in the shock-layer flow over a time scale on the order of microseconds. When the perturbation reached the bow shock, its shape was altered, and the standoff increased by up to 25%.

We have begun to formulate a high-fidelity physical model of the energy transfer process in the pulsed surface dielectric barrier discharge. For simplicity, we have focused in the present work on a planar geometry; experimental evidence shows that a nearly one-dimensional discharge can occur at relatively low pressures.²¹ Using coupled modeling of the plasma and compressible flow in a one-dimensional geometry for conditions representative of the stagnation region of the Mach 5 cylinder flow experiments, we are studying the dominant physical effects, including energy thermalization kinetics and compression wave formation and propagation.

To this end, a reduced plasma kinetic model (23 species and 50 processes) was developed first by carrying out a sensitivity analysis of a zero-dimensional plasma computation with an extended chemical kinetic model (46 species and 395 processes).²² Transient, one-dimensional discharge computations were then carried out using the reduced kinetic model, incorporating conservation equations for each species, a self-consistent computation of the electric potential using the Poisson equation, and a mass-averaged gas dynamic formulation for the bulk gas motion. This paper presents the major results of these calculations, for conditions corresponding to the cylinder flow experiments.

II. Physical Model

This section presents the chemical kinetics model and the conservation laws governing each species, the bulk gas, and the electrodynamics. There are two main differences between the present approach and other recent studies of nanosecond pulse discharges in air.^{19,23–26} First, the present model emphasizes the chemical kinetics of energy storage and thermalization. Second, in place of a traditional drift-diffusion model under the local field approximation, a more detailed model of the charged particle motion was employed here to try to capture some of the nonlocal effects, and to directly address the transfer of momentum and energy between the charged particles and neutrals.

A. Reduced Kinetic Model

A reduced chemical kinetics model²² was developed to identify the dominant species and reactions affecting the energy balance and the rate of thermalization in the discharge, and to minimize the computational cost of the transient, one-dimensional calculations that will be presented here. To obtain the reduced kinetic model, we applied a sensitivity analysis to a detailed, transient, zero-dimensional air plasma model used in previous work.²⁷ The full air plasma model was based on the model developed by Kossyi et al.²⁸ The main criterion for the sensitivity analysis was the effect of individual processes on the time-dependent energy fraction thermalized after the discharge pulse. The species included in the model are given in Table 1 and the reaction mechanism is listed in Table 2.

The reduced model includes the following species: molecular nitrogen and oxygen, atomic nitrogen and oxygen, ozone, nitric oxide, electrons, three species of ions, five electronically excited neutral species, and eight vibrationally excited neutrals. The reaction mechanism includes electron impact reactions (Reactions 1-10 and 43-50), reactions with neutral radicals (Reactions 11-17), quenching reactions and other transitions (Reactions 18-32), charge exchange reactions (Reactions 33-34), and electron-ion recombination (Reactions 35-42). Rate coefficient curve fits for most of the reactions are given in Table 2, with the remaining coefficients plotted in Fig. 1.

For the high reduced-electric-fields considered here, the rate of electron impact ionization greatly exceeds the rate of electron attachment, and processes involving negative ions do not affect the energy balance. Thus they are omitted from the model.

Further, the model also omits vibrational relaxation, which would occur over time scales much longer than those considered in the simulations. For example, for a temperature of 300 K and a pressure of 0.05 atm, the characteristic time scale for vibrational-translational relaxation of vibrationally excited nitrogen by oxygen atoms²⁹ is about 200 μ s. The time scales of interest in the present simulations are more than an order of

magnitude shorter than this.

In developing the model, zero-dimensional Boltzmann equation calculations were carried out with a steady, two-term expansion of the electron energy distribution function of the plasma electrons.³⁰ These calculations employed experimental cross sections of electron impact electronic excitation, dissociation, ionization, and dissociative attachment processes.^{31,32} The rate coefficients of the electron impact processes, as functions of the electron temperature T_e , were derived from the point Boltzmann solutions by averaging the cross sections over the electron energy distribution function. The results of these calculations are summarized in Fig. 1.

Extremely high reduced electric fields are present in the cathode sheath. Since the sheath is essentially particle-free, the critical region for accurate modeling of the discharge under the present conditions is actually the vicinity of the cathode sheath edge, where significant ionization is present and the reduced electric field is less than 1000 Td.

As a test of the validity of the model, we computed the Townsend ionization coefficient $\alpha/N = k_i/u_e$ for nitrogen using the point Boltzmann solver, and compared the results to the experimental data of Haydon and Williams.³³ The results are shown in Fig. 2. The solid line represents the results of the Boltzmann calculations, and the symbols indicate the experimental data. Error bars are included on the experimental points, representing a tolerance of three times the experimental standard deviation. Error bars are omitted for those points where the experimental uncertainty is on the order of the symbol size.

For reduced electric fields below about 1000 Td, the calculations and measurements agree within the experimental uncertainty (5%-17%). For fields between 1000 Td and 3000 Td, the Boltzmann solution is about 10% higher than the experimental data. Only above 3000 Td does the error become substantial. Thus the level of uncertainty in the present model is typical of continuum electrical discharge computations. Moreover, in PIC-MCC (particle-in-cell, Monte-Carlo collision) computations of streamers in air, Chanrion and Neubert³⁴ found that the reduced electric field had to exceed 1000 Td for runaway electrons to be observed.

Although fields higher than 1000 Td were observed in the present calculations, those regions were essentially free of charged particles. At the location of peak charged particle number density, the reduced electric field ranged from about 50 Td at 5 kV input amplitude to 130 Td at 27 kV input amplitude. Thus the physical model for ionization at the sheath edge is sufficiently accurate to permit basic parametric studies of the nanosecond-pulse, dielectric barrier discharge.

B. Governing Equations

Rather than use the traditional drift-diffusion (one-moment) model for charged particle motion, here we chose to employ the more complex five-moment model³⁵⁻⁴⁰ in order capture nonlocal effects, and to directly address the transfer of momentum and energy between the charged particles and neutrals.

Mass, momentum, and energy conservation equations were solved for each charged species:

$$\frac{\partial}{\partial t}(m_s n_s) + \nabla \cdot (m_s n_s \mathbf{v}_s) = m_s \omega_s \quad (1)$$

$$\frac{\partial}{\partial t}(m_s n_s \mathbf{v}_s) + \nabla \cdot (m_s n_s \mathbf{v}_s \mathbf{v}_s + p_s \mathbf{I}) = \nabla \cdot \boldsymbol{\tau}_s + q_s n_s \mathbf{E} + \mathbf{A}_s \quad (2)$$

$$\frac{\partial}{\partial t}[m_s n_s \mathcal{E}_s] + \nabla \cdot [m_s n_s \mathbf{v}_s \mathcal{E}_s + p_s \mathbf{v}_s] = \nabla \cdot [\boldsymbol{\tau}_s \cdot \mathbf{v}_s - \mathbf{Q}_s] + q_s n_s \mathbf{v}_s \cdot \mathbf{E} + M_s \quad (3)$$

The mass per particle of each species is denoted as m_s , and the corresponding charge per particle is q_s . The species number density is n_s , the velocity is \mathbf{v}_s , the total energy is $\mathcal{E}_s = \epsilon_s + \frac{1}{2}v_s^2$, the internal energy is ϵ_s , and the pressure is p_s . The electric field is \mathbf{E} . Here ω_s is the rate of production of particles in chemical reactions, \mathbf{A}_s is the momentum exchange in collisions, and M_s is the energy exchange. The species shear stress is $\boldsymbol{\tau}_s$ and the species heat flux is \mathbf{Q}_s .

The pressure is found from $p_s = n_s k_B T_s$, where k_B is the Boltzmann constant and T_s is the translational temperature. The internal energy per particle is assumed to have the form $m_s \epsilon_s = \mathcal{H}_s^0 + k_B(T_s - T^0)/(\gamma_s - 1)$, where γ_s is the ratio of specific heats and \mathcal{H}_s^0 is the heat of formation per particle of species- s . Values for the heat of formation of each species are given in Table 1.

For the neutral species, a diffusion equation formulation was used:

$$\frac{\partial n_s}{\partial t} + \nabla \cdot \left(n_s \mathbf{w} - \frac{D_s}{k_B T_n} \nabla p_s \right) = \omega_s \quad (4)$$

where D_s is the diffusion coefficient and \mathbf{w} is the mass-averaged velocity.

For the gas as a whole, a mass-averaged formulation was employed:

$$\frac{\partial \rho}{\partial t} + \nabla \cdot (\rho \mathbf{w}) = 0 \quad (5)$$

$$\frac{\partial}{\partial t} (\rho \mathbf{w}) + \nabla \cdot (\rho \mathbf{w} \mathbf{w} + p \mathbf{I}) = \nabla \cdot \boldsymbol{\tau} + \zeta \mathbf{E} \quad (6)$$

$$\frac{\partial}{\partial t} (\rho \mathcal{E}) + \nabla \cdot (\rho \mathbf{w} \mathcal{E} + p \mathbf{w}) = \nabla \cdot (\boldsymbol{\tau} \cdot \mathbf{w} - \mathbf{Q}) + \mathbf{E} \cdot \mathbf{j} \quad (7)$$

Here ρ is the overall density, p is the overall pressure, ζ is the space charge, and \mathbf{j} is the electric current. The diffusion velocity for each species is $\mathbf{U}_s = \mathbf{v}_s - \mathbf{w}$, $\rho \mathcal{E} = \rho \epsilon + \frac{1}{2} \rho w^2 + \sum_s \frac{1}{2} m_s n_s U_s^2$ is the total energy of the bulk gas flow, and ϵ is the total internal energy per unit mass.

The formulation allows for the interaction of the discharge with the bulk gas flow through both a body force and heating. Note that the energy delivered to the bulk gas by the electric field is initially apportioned between internal energy, thermal energy, and kinetic energy. The portion that goes into internal energy is set by the chemical kinetic model, which also allows for chemical energy to thermalize over time.

A separate temperature was computed for each charged species, but a single translational temperature was assigned to all neutral species. The neutral translational temperature T_n was determined by subtracting the flow kinetic energy and charged particle thermal energy from the total energy $\rho \mathcal{E}$, then solving the resulting expression for neutral gas energy for the translational temperature.

The diffusive fluxes for the overall gas are:

$$\boldsymbol{\tau} = \sum_s (\tau_s - m_s n_s \mathbf{U}_s \mathbf{U}_s) \quad (8)$$

$$\mathbf{Q} = \sum_s \left[\mathbf{Q}_s + m_s n_s \mathbf{U}_s \left(h_s + \frac{1}{2} U_s^2 \right) - \tau_s \cdot \mathbf{U}_s \right] \quad (9)$$

The summations in (8)-(9) include separate flux terms for each charged species, but the fluxes for the neutral species were combined in a single representative term for air. Note that we have retained a number of terms involving the diffusion velocity that are often neglected in the mass-averaged formulation. In particular, the electron heat conduction and energy convected by the electron diffusion flux make significant contributions to the total energy balance near the edge of the cathode sheath.

The Poisson equation was employed to compute the electric potential:

$$\nabla^2 \phi = -\zeta / \epsilon_0 \quad (10)$$

where ϵ_0 is the permittivity of free space. The electric field was found from $\mathbf{E} = -\nabla \phi$.

C. Closure Models

In the equation set (1)–(3), closure models are needed for the collision source terms, the viscous stress tensor, and the heat flux vector. First we consider the elastic and inelastic components of the momentum exchange term $\mathbf{A}_s = \mathbf{A}_s^E + \mathbf{A}_s^I$ and the energy exchange term $M_s = M_s^E + M_s^I$.

Because the gas is assumed to be weakly ionized, the primary elastic collisions are with neutral particles. The following models are used for the elastic components of the collision source terms^{41,42} for the charged particles:

$$\mathbf{A}_s^E = -n_s m_s \nu_s (\mathbf{v}_s - \mathbf{v}_n) \quad (11)$$

$$M_s^E = -n_s \frac{m_s \nu_s}{m_s + m_n} [3k_B (T_s - T_n) + (\mathbf{v}_s - \mathbf{v}_n) \cdot (m_s \mathbf{v}_s + m_n \mathbf{v}_n)] \quad (12)$$

Here ν_s is the rate of collision with the neutrals, and m_n is an average particle mass for the neutrals. The neutral translational temperature T_n was described earlier, and $\mathbf{v}_n \approx \mathbf{w}$ is the mass-averaged velocity of the neutrals.

Inelastic momentum and energy exchange terms, corresponding to the reaction mechanism listed in Table 2, were also included in the closure model. A reaction- r in the kinetic model can be expressed

symbolically in the form:

$$\sum_{s=1}^N \nu'_{rs} \mathcal{M}_s \rightarrow \sum_{s=1}^N \nu''_{rs} \mathcal{M}_s \quad (13)$$

where ν'_{rs} and ν''_{rs} are the stoichiometric coefficients for the reactants and products and \mathcal{M}_s is the chemical symbol for species- s . Using the law of mass action,⁴³ the rate of production of species- s can be expressed as:

$$\omega_s = \sum_r (\nu''_{rs} - \nu'_{rs}) k_r \prod_{t=1}^N n_t^{\nu'_{rt}} \quad (14)$$

where k_r is the reaction-rate constant.

The form for the inelastic momentum source terms was $\mathbf{A}_s^I = m_s \omega_s \mathbf{v}_s$ for all species, and the energy source term for the ions was $M_s^I = m_s \omega_s \mathcal{E}_s$. A more complex energy exchange term was necessary for the electrons:

$$M_s^I = m_s \omega_s \mathcal{E}_s - \sum_r R_r \Delta H_{rs} \quad (15)$$

Here $R_r = k_r \prod_{s=1}^N n_s^{\nu'_{rs}}$ is the rate of progress of reaction- r and ΔH_{rs} is the corresponding energy loss for species- s . The energy loss includes the cost of heating the electrons to the average electron temperature, and is given for each reaction in Table 3.

For a plasma in a uniform electric field, as considered in the Boltzmann solutions used to establish the rates of the electron impact reactions, overall energy conservation reduces to balance between the work done by the electric field and the energy exchange in collisions. This balance was checked for consistency for both the electron (3) and total (7) energy equations, and an error of no more than a few percent was observed over a range of electron temperatures up to 100 eV.

For the flux terms, it was assumed that the viscous term had a Newtonian form, with Stokes hypothesis applied, and that the heat flux followed Fourier's law:

$$\boldsymbol{\tau}_s = \mu_{vs} \left[(\nabla \mathbf{v}_s) + (\nabla \mathbf{v}_s)^T - \frac{2}{3} \nabla \cdot \mathbf{v}_s \mathbf{I} \right] \quad (16)$$

$$\mathbf{Q}_s = -k_s \nabla T_s \quad (17)$$

where μ_{vs} is the viscosity and k_s is the thermal conductivity for species- s .

D. Transport Properties

The viscosity and thermal conductivity of the neutrals were found from standard correlations for air.⁴⁴ The ion-neutral collision rate was determined as follows:⁴⁵

$$\nu_s/N = \sigma_s \sqrt{\frac{8k_B T_s}{\pi m_s} + |\mathbf{v}_s - \mathbf{v}_n|^2} \quad (18)$$

where σ_s is an effective collision cross-section and N is the overall number density. The collision cross-sections used for each species are given in Table 1; the values were determined from mobility and diffusion coefficient data in the literature.⁴⁵⁻⁵¹ As discussed previously, the collision rate for the electrons was determined from a point Boltzmann solution as a function of electron temperature $\nu_e/N = f(T_e)$, and is shown in Fig. 1.

The relationship between the collision rate and the transport coefficients is as follows:

$$D_s = \frac{k_B T_s}{m_s \nu_s} \quad (19)$$

$$\mu_{vs} = \frac{2}{3} n_s m_s D_s \quad (20)$$

$$k_s = \frac{5}{2} k_B n_s D_s \quad (21)$$

The forms for the viscosity and thermal conductivity correspond to a Lewis number of unity and a Prandtl number of 2/3. Note that the viscosity and thermal conductivity coefficients are proportional to number density. These transport properties are small for the low charged particle number densities in the cathode sheath, but become significant near the sheath edge.

III. Numerical Implementation

This section describes the numerical algorithm and boundary conditions. In short, an implicit, second-order upwind scheme was employed, along with standard boundary conditions for the dielectric surfaces.

A. Numerical Methods

The calculations were carried out using the Air Force Research Laboratory computer code HOPS (Higher Order Plasma Solver), which includes several physical models and numerical schemes.^{22,52} Here, the physical model consisting of (1)-(7) and (10) was solved using an implicit, second-order, upwind formulation. The equations were solved in a nondimensional form that has been described in previous papers.⁵³

Time integration of the conservation equations (1)-(7) was carried out using a second-order implicit scheme, based on a three-point backward difference of the time terms. The formulation is similar to the standard technique of Beam and Warming,⁵⁴ but is adapted here to a multi-fluid formulation with different models for particle motion. The solution was time accurate, with all equations advanced with the same time step.

Approximate factoring and quasi-Newton subiterations were employed. The implicit terms were linearized in the standard ‘thin layer’ manner. The implicit terms were evaluated with second-order spatial accuracy, yielding a block tridiagonal system of equations for each factor. The species were loosely coupled, limiting the rank of the flux Jacobian matrices to the order of the moment model (one for the diffusion equation formulation, five for the charged particles and overall conservation equations). The resulting equations were solved using a standard block tridiagonal solver, and the change in the solution vector of conserved variables was driven to zero by the subiteration procedure at each time step. Three applications of the flow solver per time-step were employed for the present work.

For the charged particles and the bulk gas, the Roe scheme⁵⁵⁻⁵⁷ was employed for the inviscid fluxes. For the diffusion model, a simple upwinding scheme was employed, based on the convection velocity. In both formulations, stability was enforced using the minmod limiter in the MUSCL formalism.⁵⁸

The Poisson equation (10) was solved at the end of each subiteration in the implicit time-marching scheme. (This procedure yields a stable time step that is comparable to that obtained using methods based on the linearization of the right-hand-side of the Poisson equation.⁵⁹) The numerical scheme was adapted from the approach described by Holst.⁶⁰ The formulation of the implicit scheme was analogous to that used for the conservation equations, with linearization of the implicit terms, approximate factoring, and an iterative procedure that drives the change in the solution to zero. The spatial derivatives were evaluated using second-order central differences, and the system was solved using a standard tridiagonal algorithm.

B. Boundary Conditions

A one-dimensional computational domain was employed to represent a double dielectric barrier discharge (Fig. 3). All the boundary conditions were enforced to second-order numerical accuracy. No-slip boundary conditions with a constant temperature wall were employed for the bulk gas. A zero wall-normal derivative was imposed for the neutral species.

Standard boundary conditions were employed for the charged particles. First, provisional conditions at the wall were determined by setting the normal derivative to zero. Then, if the ion flow was away from the boundary, the ion flux was set to zero and the ion temperature was set to the wall temperature. For electron flow from the wall into the domain, the normal component of the electron velocity was set to that required to satisfy secondary emission, and the electron temperature was set to a specified emission temperature (here, 1 eV).

Simplified boundary conditions were employed to model a thin dielectric electrode coating.⁴⁹ The dielectric layer was assumed to be sufficiently thin to be approximated a linear potential profile (uniform electric field \mathbf{E}_d). The electric field inside the dielectric was related to the electric field \mathbf{E} at the surface through the relation $\epsilon_0\mathbf{E} - \epsilon_r\epsilon_0\mathbf{E}_d = \sigma\mathbf{n}$, where σ is the surface charge density and \mathbf{n} is the unit normal vector pointing into the computational domain. The surface charge was determined by integrating $\partial\sigma/\partial t = -\mathbf{j} \cdot \mathbf{n}$ for each surface point,⁶¹ using a time-marching scheme analogous to that of the main governing equations.

C. Two-Stage Formulation

For computational efficiency, the calculations were carried out in two stages. The first stage encompassed the first 400 ns of the discharge. For this stage, the full physical model discussed above was employed. Since electromagnetic effects and charged particle motion become negligible after the input pulse dies away (after about 24 ns), in the second stage of the computations (0.4 μ s to 100.4 μ s), the electric field was set to zero and neutrality was enforced by appropriately setting the electron number density. This two-stage approach resulted in a substantial savings in computational cost, and tests comparing this approach to the full formulation showed a negligible difference.

IV. Results

Calculations were carried out for a one-dimensional discharge under conditions representative of the stagnation region of a Mach 5 cylinder flow experiment described in a previous publication.²⁰ The corresponding stagnation conditions were 4.74 kPa (36 Torr) and 310.3 K; for each case in the calculations discussed below, the initial, uniform state of the neutral gas was set to these values.

The configuration considered here is illustrated in Fig. 3. The problem is one-dimensional. In the simulations, the right electrode was grounded, and the left electrode was powered with the input signal $V_s = -V_0 \exp[-(t - t_0)^2/\tau^2]$. For the present calculations, the input signal parameters were $V_0 = 5$ kV to 27 kV, $\tau = 3$ ns, and $t_0 = 12$ ns.

Both electrodes were assumed to be covered with a $d = 1$ mm thick dielectric coating, with a relative dielectric constant of $\epsilon_r = 3.8$, chosen to be representative of fused quartz. The discharge gap (distance between the dielectric surfaces) was taken to be $L = 2$ mm. The secondary emission coefficient was $\gamma_{sem} = 0.05$.

The initial mole fraction of the electrons and each of the neutral minor species was taken to be 1×10^{-10} . The number densities of the vibrational states of N_2 were set to an equilibrium distribution for the initial temperature. The mole fraction for each ion species was equal, and set so that the space charge was zero. The initial electric field was zero. The ion, electron, and neutral temperatures were set to 310.3 K, and all velocities were set to zero.

For the calculations presented here, a uniform grid of 1001 points across the gap was employed ($\Delta x = 2 \mu$ m). Grid resolution studies presented in a previous paper²² indicate that this level of grid resolution is sufficient for this problem.

The time step for the Stage 1 calculations (see Sec. III.C) was taken to be 0.5 ps for the 5 kV case. The minimum chemical kinetic time scale and dielectric relaxation time scale were both about 20 ps, and the minimum electron diffusion time scale was about 2.5 ps, so the time-evolution of the discharge was well-resolved in the calculations. The corresponding time step for the 10 kV and 20 kV cases was 0.25 ps, and for the 27 kV case it was 0.125 ps. For the Stage 2 calculations, the time step was taken to be 0.5 ns for all cases.

A. Baseline Case

A baseline case with $V_0 = 5$ kV was studied first. The general structure of the discharge is shown in figures 4-5, which show profiles of number density, potential, velocity, and temperature at times corresponding to the peak in the input voltage (12 ns, Fig. 4) and the effective end of the input signal (24 ns, Fig. 5). The cathode sheath is evident at the left in the figures as a region largely free of charged particles. There is a relatively large electric field in the sheath, resulting from the region of space charge at the sheath edge ($x/L \approx 0.3$).

Note that the electron velocity and temperature at the left boundary are set by secondary emission. At the peak of the input signal (12 ns), ion velocities reach $\sim 10^3$ m/s in the sheath, and electron velocities $\sim 10^6$ m/s. Corresponding temperatures reach ~ 1 eV for the ions and 50 eV for the electrons. Although these values are quite high, the charged particle density is extremely low in the left sheath, and there is essentially no conduction current or energy storage there. Despite the high dimensional velocities, it should be noted that the maximum electron Mach number is about 0.7, and the maximum ion Mach number lies in the range of 1.0-1.6.

As the input signal dies away, the discharge enters a dual-cathode regime,⁴ as seen in Fig. 5 at 24 ns. At both boundaries, ions travel toward the wall, and electrons away. At this stage, the space charge in the left sheath has decayed significantly, but the right sheath is quite prominent.

Note the qualitative differences between the left and right sheaths. The left sheath is formed during the input voltage rise by way of an ionization wave propagating into a very weakly pre-ionized plasma. The right sheath forms during the voltage fall, in a region with significant existing ionization. Its characteristics are similar to those of sheaths at a negative electrode in a DC or RF discharge. In particular, there is significant ion current in the right sheath, in contrast to the absence of conduction current in the left sheath.

B. Acoustic Waves

The interaction between the discharge and the bulk gas flow occurs through the source terms in Eqs. (6)-(7). Terms of interest include the body force $\zeta\mathbf{E}$, the rate of work done by the body force $\zeta\mathbf{E}\cdot\mathbf{w}$, and the total electromagnetic power $\mathbf{E}\cdot\mathbf{j}$. Maximum values of these terms occur near the edge of the left sheath at the peak of the input waveform, and near the edge of the right sheath as the input waveform decays. The body force is always directed toward the electrodes, and tends to be stronger for the left sheath. For the $V_0 = 5$ kV input amplitude, the order of magnitude of the terms was as follows: peak body force 10^5 N/m³, rate of work done by body force 10^4 W/m³, and total electromagnetic power 10^{10} W/m³. The corresponding values for $V_0 = 27$ kV were: peak body force 10^7 N/m³, rate of work done by body force 10^7 W/m³, and total electromagnetic power 10^{11} W/m³. (These large values exist only for time scales on the order of the width of the input waveform, and for spatial scales on the order of the discharge volume.) Since the total power is four to six orders of magnitude larger than the rate of work done, acoustic waves that appear in the discharge must primarily be a result of thermal energy release.

The formation of acoustic waves from the heat release is illustrated in Fig. 6, which shows temperature and velocity profiles at several times for the 5 kV and 27 kV cases. In both cases, heating at the cathode sheath edge ($x/L \approx 0.3$) generates waves that propagate away from that location. Similarly, heating near the right boundary creates a wave that travels into the domain.

Focusing on the vicinity of the left sheath edge at $0.4 \mu\text{s}$ for the 5 kV case (red curve in Fig. 6b), we note an asymmetry in the waveform that is probably a result of the left-directed body force. The velocity of the left-running wave is about 60% higher than the that of the right-running wave. The corresponding difference for the 27 kV case (red curve in Fig. 6d) is about 40%. Nonetheless, the body force has a relatively small influence on the formation of the acoustic waves.

The results are qualitatively similar for all the cases examined here, with the wave amplitude and speed increasing with the amplitude of the input signal. The wave speeds are nearly sonic for all cases; the Mach number does not exceed 1.08. (The sound speed is 353 m/s for air at 310.3 K, and the wave speeds lie in the range of 350–380 m/s.) At later stages in the computations (not shown), the waves reflect from the solid boundaries, producing complex wave patterns.

These computational results are consistent with the waves emanating from the cathode and anode in a pulsed CO₂ laser observed by Pugh et al.¹³ using interferometry. Those authors noted both generation of waves by discharge heating and reflection of the resulting waves from solid boundaries. The configuration in the Mach 5 cylinder flow experiments²⁰ was somewhat more complicated, but similar results were obtained. A weak shock formed near the edge of the exposed electrode and propagated into the shock layer flow. The results of the present calculations are qualitatively consistent with those of both experimental studies. Further, wave speeds extracted from the computational results shown in Fig. 6d lie in the range of 350–380 m/s, in general agreement with the value of 375 m/s measured in the Mach 5 cylinder flow experiments.

V. Summary and Conclusions

Numerical calculations were carried out to examine the physics of the operation of a nanosecond-pulse, dielectric barrier discharge in a configuration with planar symmetry. This simplified configuration was chosen as a vehicle to develop a physics-based nanosecond discharge model, including realistic air plasma chemistry and compressible bulk gas flow. Discharge parameters (temperature, pressure, and input waveform) were selected to be representative of recent experiments on bow shock control with a nanosecond discharge in a Mach 5 cylinder flow.

The computational results qualitatively reproduce many of the features observed in the experiments, including the rapid thermalization of the input electrical energy and the consequent formation of weak shock waves. Despite the simplifications employed in the calculations, the computed translational temperature rise (40 K) and nitrogen vibrational temperature rise (370 K) were of the same order of magnitude as those

measured experimentally (50 K and 500 K, respectively). The results illustrate how input electrical energy is rapidly transformed (over roughly 1 ns) at breakdown into ionization products, dissociation products, and electronically excited particles, and how thermalization occurs over a relatively longer time-scale (roughly 10 μ s). The quenching of electronically excited states and electron-ion recombination make roughly equal contributions to the thermalization of stored chemical energy.

This work represents a first step towards detailed modeling of the nanosecond-pulse dielectric barrier discharge actuator. This type of actuator shows promise for high-speed flow control, and accurate numerical modeling will contribute the optimization of these devices. In ongoing work, we are extending the model to multiple dimensions, which should allow a more realistic representation of the electric field and better quantitative comparison with experiment.

Acknowledgments

This project was sponsored in part by the Air Force Office of Scientific Research (monitored by F. Fahroo, AFOSR/RSL), and by a grant of High Performance Computing time from the Air Force Research Laboratory Major Shared Resource Center. Work at The Ohio State University was funded in part by the Chief Scientist Innovative Research Fund (CSIRF) of the Air Force Research Laboratory Air Vehicles Directorate (AFRL/RB). The authors would like to thank M. N. Shneider for helpful discussions. Cleared for public release, distribution unlimited (88ABW-2012-6103).

References

- ¹Lieberman, M. A. and Lichtenberg, A. J., *Principles of Plasma Discharges and Materials Processing*, J. Wiley, New York, 1994.
- ²Vasilyak, L. M., Kostyuchenko, S. V., Kudryavtsev, N. N., and Filyugin, I. V., "Fast Ionisation Waves under Electrical Breakdown Conditions," *Physics-Uspekhii*, Vol. 37, No. 4, 1994, pp. 247–269.
- ³Fridman, A. and Kennedy, L. A., *Plasma Physics and Engineering*, Taylor and Francis, New York, 2004.
- ⁴Macheret, S. O., Shneider, M. N., and Miles, R. B., "Modeling of Air Plasma Generation by Repetitive High-Voltage Nanosecond Pulses," *IEEE Transactions on Plasma Science*, Vol. 30, No. 3, 2002, pp. 1301–1314.
- ⁵Opaitis, D. F., Likhanskii, A. V., Neretti, G., Zaidi, S., Shneider, M. N., Miles, R. B., and Macheret, S. O., "Experimental Investigation of Dielectric Barrier Discharge Plasma Actuators Driven by Repetitive High-Voltage Nanosecond Pulses with DC or Low Frequency Sinusoidal Bias," *Journal of Applied Physics*, Vol. 104, 2008, pp. 043304.
- ⁶Roupassov, D. V., Nikipelov, A. A., Nudnova, M. M., and Starikovskii, A. Y., "Flow Separation Control by Plasma Actuator with Nanosecond Pulsed-Periodic Discharge," *AIAA Journal*, Vol. 47, No. 1, 2009, pp. 168–185.
- ⁷(Udagawa), K. T., Zuzeev, Y., Lempert, W. R., and Adamovich, I. V., "Characterization of a Surface Dielectric Barrier Discharge Plasma Sustained by Repetitive Nanosecond Pulses," *Plasma Sources Science and Technology*, Vol. 20, 2011, pp. 055009.
- ⁸Little, J., Takashima, K., Nishihara, M., Adamovich, I., and Samimy, M., "Separation Control with Nanosecond-Pulse-Driven Dielectric Barrier Discharge Plasma Actuators," *AIAA Journal*, Vol. 50, No. 2, 2012, pp. 350–365.
- ⁹Murray, R. C., Zaidi, S. H., Carraro, M. R., Vasilyak, L. M., Macheret, S. O., Shneider, M. N., and Miles, R. B., "Magnetohydrodynamic Power Generation Using Externally Ionized, Cold, Supersonic Air as Working Fluid," *AIAA Journal*, Vol. 44, No. 1, 2006, pp. 119–127.
- ¹⁰Adamovich, I. V., Lempert, W. R., Nishihara, M., Rich, J. W., and Utkin, Y. G., "Repetitively Pulsed Nonequilibrium Plasmas for Magnetohydrodynamic Flow Control and Plasma-Assisted Combustion," *Journal of Propulsion and Power*, Vol. 24, No. 6, 2008, pp. 1198–1215.
- ¹¹Pancheshnyi, S. V., Lacoste, D. A., Bourdon, A., and Laux, C. O., "Ignition of Propane-Air Mixtures by a Repetitively Pulsed Nanosecond Discharge," *IEEE Transactions on Plasma Science*, Vol. 34, No. 6, 2006, pp. 2478–2487.
- ¹²Sun, W., Uddi, M., Won, S. H., Ombrello, T., Carter, C., and Ju, Y., "Kinetic Effects of Non-Equilibrium Plasma-Assisted Methane Oxidation on Diffusion Flame Extinction Limits," *Combustion and Flame*, Vol. 159, 2012, pp. 221–229.
- ¹³Pugh, E. R., Wallace, J., Jacob, J. H., Northam, D. B., and Daugherty, J. D., "Optical Quality of Pulsed Electron-Beam Sustained Lasers," *Applied Optics*, Vol. 13, No. 11, 1974, pp. 2512–2517.
- ¹⁴Aleksandrov, V. V., Koterov, V. N., Pustovalov, V. V., Soroka, A. M., and Suchkov, A. F., "Space-Time Evolution of the Cathode Layer in Electron-Beam-Controlled Lasers," *Soviet Journal of Quantum Electronics*, Vol. 8, No. 1, 1978, pp. 59–63.
- ¹⁵Popov, N. A., "Investigation of the Mechanism for Rapid Heating of Nitrogen and Air in Gas Discharges," *Plasma Physics Reports*, Vol. 27, No. 10, 2001, pp. 886–896.
- ¹⁶Flitti, A. and Pancheshnyi, S., "Gas Heating in Fast Pulsed Discharges in N₂-O₂ Mixtures," *The European Physical Journal: Applied Physics*, Vol. 45, 2009, pp. 21001.
- ¹⁷Aleksandrov, N. L., Kindysheva, S. V., Nudnova, M. N., and Starikovskiy, A. Y., "Mechanism of Ultra-Fast Heating in a Non-Equilibrium Weakly Ionized Air Discharge Plasma in High Electric Fields," *Journal of Physics D: Applied Physics*, Vol. 43, 2010, pp. 255201.
- ¹⁸Popov, N., "Fast Gas Heating in a Nitrogen-Oxygen Discharge Plasma: I. Kinetic Mechanism," *Journal of Physics D: Applied Physics*, Vol. 44, 2011, pp. 285201.

- ¹⁹Unfer, T. and Boeuf, J. P., “Modelling of a Nanosecond Surface Discharge Actuator,” *Journal of Physics D: Applied Physics*, Vol. 42, 2009, pp. 194017.
- ²⁰Nishihara, M., Takashima, K., Rich, J. W., and Adamovich, I. V., “Mach 5 Bow Shock Control by a Nanosecond Pulse Surface Dielectric Barrier Discharge,” *Physics of Fluids*, Vol. 23, 2011, pp. 066101.
- ²¹Kirpichnikov, A. A. and Starikovskii, A. Y., “Nanosecond Pulse Discharge – Always Uniform?” *IEEE Transactions on Plasma Science*, Vol. 36, No. 4, 2008, pp. 898–899.
- ²²Poggie, J., Bisek, N. J., Adamovich, I. V., and Nishihara, M., “Numerical Simulation of Nanosecond-Pulse Electrical Discharges,” AIAA Paper 2012-1025, American Institute of Aeronautics and Astronautics, Reston, VA, January 2012.
- ²³Likhanskii, A. V., Shneider, M. N., Macheret, S. O., and Miles, R. B., “Modeling of Dielectric Barrier Discharge Plasma Actuators Driven by Nanosecond Pulses,” *Physics of Plasmas*, Vol. 14, 2007, pp. 073501.
- ²⁴Breden, D. and Raja, L. L., “Gas Heating Effects in a Nanosecond-Pulse Streamer Discharge Interacting with a Supersonic O₂-H₂ Flow,” *IEEE Transactions on Plasma Science*, Vol. 39, No. 11, 2011, pp. 2250–2251.
- ²⁵Che, X., Shao, T., Nie, W., and Yan, P., “Numerical Simulation on a Nanosecond-Pulse Surface Dielectric Barrier Discharge Actuator in Near Space,” *Journal of Physics D: Applied Physics*, Vol. 45, 2012, pp. 145201.
- ²⁶Wang, C.-C., “Energy and Force Prediction for a Nanosecond Pulsed Dielectric Barrier Discharge Actuator,” *Journal of Applied Physics*, Vol. 111, No. 10, 2012, pp. 103302.
- ²⁷Uddi, M., Jiang, N., Adamovich, I. V., and Lempert, W. R., “Nitric Oxide Density Measurements in Air and Air/Fuel Nanosecond Pulse Discharges by Laser Induced Fluorescence,” *Journal of Physics D: Applied Physics*, Vol. 42, 2009, pp. 075205.
- ²⁸Kossyi, I. A., Kostinsky, A. Y., Matveyev, A. A., and Silakov, V. P., “Kinetic Scheme of the Nonequilibrium Discharge in Nitrogen-Oxygen Mixtures,” *Plasma Sources Science and Technology*, Vol. 1, 1992, pp. 207–220.
- ²⁹McNeal, R. J., Jr., M. E. W., and Cook, G. R., “Quenching of Vibrationally Excited N₂ by Atomic Oxygen,” *Chemical Physics Letters*, Vol. 16, No. 3, 1972, pp. 507–510.
- ³⁰Huxley, L. G. H. and Crompton, R. W., *The Diffusion and Drift of Electrons in Gases*, Wiley, New York, 1974.
- ³¹Itikawa, Y., Hayashi, M., Ichimura, A., Onda, K., Sakimoto, K., Takayanagi, K., Nakamura, M., Nishimura, M., and Takayanagi, T., “Cross Sections for Collisions of Electrons and Photons with Nitrogen Molecules,” *Journal of Physical and Chemical Reference Data*, Vol. 16, 1986, pp. 985–1010.
- ³²Itikawa, Y., Ichimura, A., Onda, K., Sakimoto, K., Takayanagi, K., Hatano, Y., Hayashi, M., Nishimura, H., and Tsurubichi, S., “Cross Sections for Collisions of Electrons and Photons with Oxygen Molecules,” *Journal of Physical and Chemical Reference Data*, Vol. 18, 1989, pp. 23–42.
- ³³Haydon, S. C. and Williams, O. M., “Combined Spatial and Temporal Studies of Ionization Growth in Nitrogen,” *Journal of Physics D: Applied Physics*, Vol. 9, 1976, pp. 523–536.
- ³⁴Chanrion, O. and Neubert, T., “A PIC-MCC Code for Simulation of Streamer Propagation in Air,” *Journal of Computational Physics*, Vol. 227, 2008, pp. 7222–7245.
- ³⁵Meyyappan, M. and Kreskovsky, J. P., “Glow Discharge Simulation Through Solutions to the Moments of the Boltzmann Transport Equation,” *Journal of Applied Physics*, Vol. 68, No. 4, 1990, pp. 1506–1512.
- ³⁶Wilcoxson, M. H. and Manousiouthakis, V. I., “Simulation of a Three-Moment Fluid Model of a Two-Dimensional Radio Frequency Discharge,” *Chemical Engineering Science*, Vol. 51, No. 7, 1996, pp. 1089–1106.
- ³⁷Chen, G. and Raja, L. L., “Fluid Modeling of Electron Heating in Low-Pressure, High-Frequency Capacitively Coupled Plasma Discharges,” *Journal of Applied Physics*, Vol. 96, No. 11, 2004, pp. 6073–6081.
- ³⁸Adamovich, I. V. and Rich, J. W., “Emission and Shock Visualization in Nonequilibrium Nitrogen Afterglow Plasma,” *Journal of Applied Physics*, Vol. 102, 2007, pp. 083303.
- ³⁹Hakim, A. and Shumlak, U., “Two-Fluid Physics and Field-Reversed Configurations,” *Physics of Plasmas*, Vol. 14, 2007, pp. 055911.
- ⁴⁰Poggie, J., Adamovich, I., Bisek, N., and Nishihara, M., “Numerical Simulation of Nanosecond-Pulse Electrical Discharges,” *Plasma Sources Science and Technology*, Vol. 22, 2012, pp. 015001.
- ⁴¹Burgers, J. M., *Flow Equations for Composite Gases*, Academic Press, New York, 1969.
- ⁴²Golant, V. E., Zhilinsky, A. P., and Sakharov, I. E., *Fundamentals of Plasma Physics*, J. Wiley, New York, 1980, Trans. K. Z. Vedeneva and V. F. Agranat.
- ⁴³Williams, F. A., *Combustion Theory*, Addison-Wesley, Menlo Park CA, 4th ed., 1988.
- ⁴⁴White, F. M., *Viscous Fluid Flow*, McGraw-Hill, New York, 2nd ed., 1991.
- ⁴⁵Mahadevan, S. and Raja, L., “Simulations of Direct-Current Air Glow Discharges at Pressures ~ 1 Torr: Discharge Model Validation,” *Journal of Applied Physics*, Vol. 107, 2010, pp. 093304.
- ⁴⁶Chen, N. H. and Othmer, D. F., “New Generalized Equation for Gas Diffusion Coefficient,” *Journal of Chemical and Engineering Data*, Vol. 7, No. 1, 1962, pp. 37–41.
- ⁴⁷Viehland, L. A. and Mason, E. A., “Transport Properties of Gaseous Ions over a Wide Energy Range, IV,” *Atomic Data and Nuclear Data Tables*, Vol. 60, 1995, pp. 37–95.
- ⁴⁸Nelson, D., Benhenni, M., Eichwald, O., and Yousfi, M., “Ion Swarm Data for Electrical Discharge Modeling in Air and Flue Gas Mixtures,” *Journal of Applied Physics*, Vol. 94, No. 1, 2003, pp. 96–103.
- ⁴⁹Deconinck, T., Mahadevan, S., and Raja, L. L., “Simulation of Direct-Current Surface Plasma Discharge Phenomena in High-Speed Flow Actuation,” *IEEE Transactions on Plasma Science*, Vol. 35, No. 5, 2007, pp. 1301–1311.
- ⁵⁰Ivanov, A. V., Takhtenberg, S., Bertram, A. K., Gershenzon, Y. M., and Molina, M. J., “OH, HO₂, and Ozone Gaseous Diffusion Coefficients,” *Journal of Physical Chemistry A*, Vol. 111, 2007, pp. 1632–1637.
- ⁵¹Breden, D. and Raja, L. L., “Simulations of Nanosecond Pulsed Plasmas in Supersonic Flow,” AIAA Paper 2009-3594, American Institute of Aeronautics and Astronautics, Reston, VA, June 2009.
- ⁵²Poggie, J., “Numerical Simulation of Direct Current Glow Discharges for High-Speed Flow Control,” *Journal of Propulsion and Power*, Vol. 24, No. 5, 2008, pp. 916–922.

- ⁵³Poggie, J., “High-Order Numerical Methods for Electrical Discharge Modeling,” AIAA Paper 2010-4632, American Institute of Aeronautics and Astronautics, Reston VA, 2011.
- ⁵⁴Beam, R. and Warming, R., “An Implicit Factored Scheme for the Compressible Navier-Stokes Equations,” *AIAA Journal*, Vol. 16, No. 4, 1978, pp. 393–402.
- ⁵⁵Morrison, J., “Flux Difference Split Scheme for Turbulent Transport Equations,” AIAA Paper 90-5251, American Institute of Aeronautics and Astronautics, Reston, VA, October 1990.
- ⁵⁶Walters, R. W., Cinnella, P., Slack, D. C., and Halt, D., “Characteristic-Based Algorithms for Flows in Thermo-Chemical Nonequilibrium,” AIAA Paper 90-0393, American Institute of Aeronautics and Astronautics, Reston, VA, January 1990.
- ⁵⁷Gaitonde, D. and Shang, J. S., “Accuracy of Flux-Split Algorithms in High-Speed Viscous Flows,” *AIAA Journal*, Vol. 31, No. 7, 1993, pp. 1215–1221.
- ⁵⁸Anderson, W. K., Thomas, J. L., and van Leer, B., “A Comparison of Finite Volume Flux Vector Splittings for the Euler Equations,” AIAA Paper 85-0122, American Institute of Aeronautics and Astronautics, Reston, VA, January 1985.
- ⁵⁹Ventzek, P. L. G., Hoekstra, R. J., and Kushner, M. J., “Two-Dimensional Modeling of High Plasma Density Inductively Coupled Sources for Materials Processing,” *Journal of Vacuum Science and Technology B*, Vol. 12, No. 1, 1994, pp. 461–477.
- ⁶⁰Holst, T. L., “Transonic Flow Computations Using Nonlinear Potential Methods,” *Progress in Aerospace Sciences*, Vol. 36, 2000, pp. 1–61.
- ⁶¹Soloviev, V. R. and Krivtsov, V. M., “Surface Barrier Discharge Modelling for Aerodynamic Applications,” *Journal of Physics D: Applied Physics*, Vol. 42, 2009, pp. 125208.

No.	Species	\mathcal{H}_s^0 (eV/particle)	σ_s (10^{-20} m^2)
1	N ₂	0	41
2	O ₂	0	39
3	O	2.58	32
4	O ₃	1.48	45
5	NO	0.94	31
6	N	4.90	38
7	O(¹ D)	4.55	32
8	N ₂ (A ³ Σ)	6.17	41
9	N ₂ (B ³ Π)	7.35	41
10	N ₂ (a ¹ Σ)	8.40	41
11	N ₂ (C ³ Π)	11.03	41
12	e ⁻	0	-
13	N ₂ ⁺	16.37	148
14	O ⁺	16.26	80
15	O ₂ ⁺	12.69	115
16	N ₂ (<i>v</i> = 1)	0.29	41
17	N ₂ (<i>v</i> = 2)	0.57	41
18	N ₂ (<i>v</i> = 3)	0.86	41
19	N ₂ (<i>v</i> = 4)	1.14	41
20	N ₂ (<i>v</i> = 5)	1.41	41
21	N ₂ (<i>v</i> = 6)	1.68	41
22	N ₂ (<i>v</i> = 7)	1.95	41
23	N ₂ (<i>v</i> = 8)	2.21	41

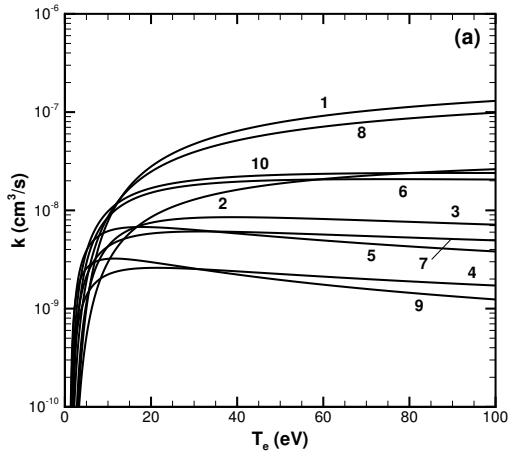
Table 1. Species included in kinetic model. Heat of formation referenced to 300 K.

No.	Reaction	Rate
1	$N_2 + e^- \rightarrow N_2^+ + e^- + e^-$	Fig. 1a
2	$O_2 + e^- \rightarrow O_2^+ + e^- + e^-$	Fig. 1a
3	$O_2 + e^- \rightarrow O + O^+ + e^- + e^-$	Fig. 1a
4	$N_2 + e^- \rightarrow N_2(A^3\Sigma) + e^-$	Fig. 1a
5	$N_2 + e^- \rightarrow N_2(B^3\Pi) + e^-$	Fig. 1a
6	$N_2 + e^- \rightarrow N_2(C^3\Pi) + e^-$	Fig. 1a
7	$N_2 + e^- \rightarrow N_2(a^1\Sigma) + e^-$	Fig. 1a
8	$N_2 + e^- \rightarrow N + N + e^-$	Fig. 1a
9	$O_2 + e^- \rightarrow O + O + e^-$	Fig. 1a
10	$O_2 + e^- \rightarrow O + O(^1D) + e^-$	Fig. 1a
11	$N + O_2 \rightarrow NO + O$	$k = 1.1 \times 10^{-14} T \exp(-3150./T)$
12	$N + NO \rightarrow N_2 + O$	$k = 1.1 \times 10^{-12} T^{0.5}$
13	$O + O_3 \rightarrow O_2 + O_2$	$k = 2.0 \times 10^{-11} \exp(-2300./T)$
14	$O + O + N_2 \rightarrow O_2 + N_2$	$k = 2.8 \times 10^{-34} \exp(720./T)$
15	$O + O + O_2 \rightarrow O_2 + O_2$	$k = 2.5 \times 10^{-31} T^{-0.63}$
16	$O + O_2 + N_2 \rightarrow O_3 + N_2$	$k = 5.6 \times 10^{-29} T^{-2.0}$
17	$O + O_2 + O_2 \rightarrow O_3 + O_2$	$k = 8.6 \times 10^{-31} T^{-1.25}$
18	$N_2(A^3\Sigma) + O_2 \rightarrow N_2 + O + O$	$k = 1.7 \times 10^{-12}$
19	$N_2(A^3\Sigma) + O_2 \rightarrow N_2 + O_2$	$k = 7.5 \times 10^{-13}$
20	$N_2(A^3\Sigma) + O \rightarrow N_2 + O(^1D)$	$k = 3.0 \times 10^{-11}$
21	$N_2(A^3\Sigma) + N_2(A^3\Sigma) \rightarrow N_2 + N_2(B^3\Pi)$	$k = 7.7 \times 10^{-11}$
22	$N_2(A^3\Sigma) + N_2(A^3\Sigma) \rightarrow N_2 + N_2(C^3\Pi)$	$k = 1.6 \times 10^{-10}$
23	$N_2(B^3\Pi) + N_2 \rightarrow N_2(A^3\Sigma) + N_2$	$k = 3.0 \times 10^{-11}$
24	$N_2(B^3\Pi) \rightarrow N_2(A^3\Sigma) + h\nu$	$k = 1.5 \times 10^5$
25	$N_2(B^3\Pi) + O_2 \rightarrow N_2 + O + O$	$k = 3.0 \times 10^{-10}$
26	$N_2(a^1\Sigma) + N_2 \rightarrow N_2 + N_2$	$k = 2.0 \times 10^{-13}$
27	$N_2(a^1\Sigma) + O_2 \rightarrow N_2 + O + O(^1D)$	$k = 2.8 \times 10^{-11}$
28	$N_2(C^3\Pi) + N_2 \rightarrow N_2(B^3\Pi) + N_2$	$k = 1.0 \times 10^{-11}$
29	$N_2(C^3\Pi) \rightarrow N_2(B^3\Pi) + h\nu$	$k = 3.0 \times 10^7$
30	$N_2(C^3\Pi) + O_2 \rightarrow N_2(A^3\Sigma) + O + O$	$k = 3.0 \times 10^{-10}$
31	$O(^1D) + N_2 \rightarrow O + N_2$	$k = 2.6 \times 10^{-11}$
32	$O(^1D) + O_2 \rightarrow O + O_2$	$k = 4.0 \times 10^{-11}$
33	$O^+ + O_2 \rightarrow O_2^+ + O$	$k = 2.0 \times 10^{-11}$
34	$N_2^+ + O_2 \rightarrow N_2 + O_2^+$	$k = 6.0 \times 10^{-11}$
35	$N_2^+ + e^- \rightarrow N + N$	$k = 8.3 \times 10^{-6} T_e^{-0.5}$
36	$O_2^+ + e^- \rightarrow O + O$	$k = 6.0 \times 10^{-5} T_e^{-1.0}$
37	$N_2^+ + e^- + e^- \rightarrow N_2 + e^-$	$k = 1.4 \times 10^{-8} T_e^{-4.5}$
38	$O_2^+ + e^- + e^- \rightarrow O_2 + e^-$	$k = 1.4 \times 10^{-8} T_e^{-4.5}$
39	$O^+ + e^- + e^- \rightarrow O + e^-$	$k = 1.4 \times 10^{-8} T_e^{-4.5}$
40	$N_2^+ + e^- + M \rightarrow N_2 + M$	$k = 3.1 \times 10^{-23} T_e^{-1.5}$
41	$O_2^+ + e^- + M \rightarrow O_2 + M$	$k = 3.1 \times 10^{-23} T_e^{-1.5}$
42	$O^+ + e^- + M \rightarrow O + M$	$k = 3.1 \times 10^{-23} T_e^{-1.5}$
43-50	$N_2(v=0) + e^- \rightarrow N_2(v=1-8) + e^-$	Fig. 1b

Table 2. Reaction mechanism. Units consistent with number densities in cm^{-3} , and temperatures in K, one-body rates in s^{-1} , two-body rates in cm^3/s , and three-body rates in cm^6/s .

No.	Reaction	$\Delta H/e$ (V)
1	$\text{N}_2 + e^- \rightarrow \text{N}_2^+ + e^- + e^-$	$16.37 + 3k_B T_e / (2e)$
2	$\text{O}_2 + e^- \rightarrow \text{O}_2^+ + e^- + e^-$	$12.69 + 3k_B T_e / (2e)$
3	$\text{O}_2 + e^- \rightarrow \text{O} + \text{O}^+ + e^- + e^-$	$18.84 + 3k_B T_e / (2e)$
4	$\text{N}_2 + e^- \rightarrow \text{N}_2(\text{A}^3\Sigma) + e^-$	6.17
5	$\text{N}_2 + e^- \rightarrow \text{N}_2(\text{B}^3\Pi) + e^-$	7.35
6	$\text{N}_2 + e^- \rightarrow \text{N}_2(\text{C}^3\Pi) + e^-$	11.03
7	$\text{N}_2 + e^- \rightarrow \text{N}_2(\text{a}^1\Sigma) + e^-$	8.40
8	$\text{N}_2 + e^- \rightarrow \text{N} + \text{N} + e^-$	9.80
9	$\text{O}_2 + e^- \rightarrow \text{O} + \text{O} + e^-$	5.17
10	$\text{O}_2 + e^- \rightarrow \text{O} + \text{O}({}^1\text{D}) + e^-$	7.14
43	$\text{N}_2(v=0) + e^- \rightarrow \text{N}_2(v=1) + e^-$	0.29
44	$\text{N}_2(v=0) + e^- \rightarrow \text{N}_2(v=2) + e^-$	0.57
45	$\text{N}_2(v=0) + e^- \rightarrow \text{N}_2(v=3) + e^-$	0.86
46	$\text{N}_2(v=0) + e^- \rightarrow \text{N}_2(v=4) + e^-$	1.14
47	$\text{N}_2(v=0) + e^- \rightarrow \text{N}_2(v=5) + e^-$	1.41
48	$\text{N}_2(v=0) + e^- \rightarrow \text{N}_2(v=6) + e^-$	1.68
49	$\text{N}_2(v=0) + e^- \rightarrow \text{N}_2(v=7) + e^-$	1.95
50	$\text{N}_2(v=0) + e^- \rightarrow \text{N}_2(v=8) + e^-$	2.21

Table 3. Energy lost by electrons in inelastic collisions.



(a) Rates of ionization and electronic excitation (Reactions 1-10).

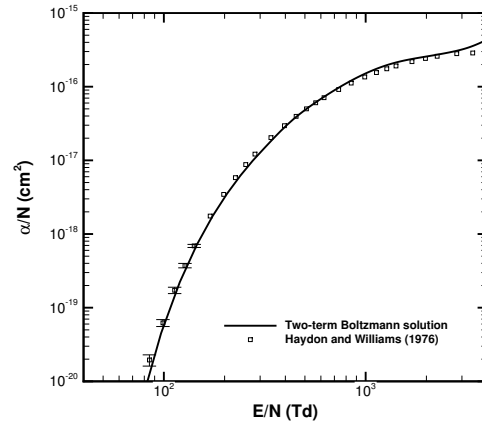
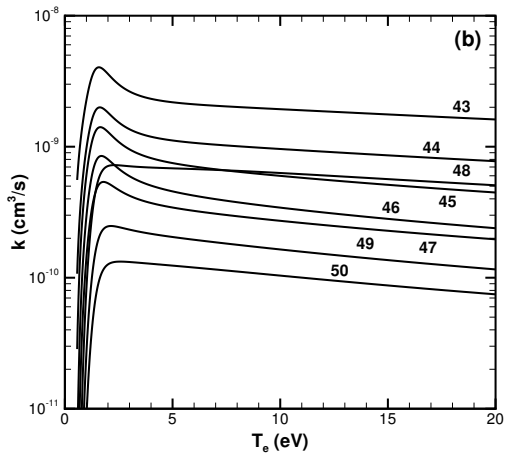
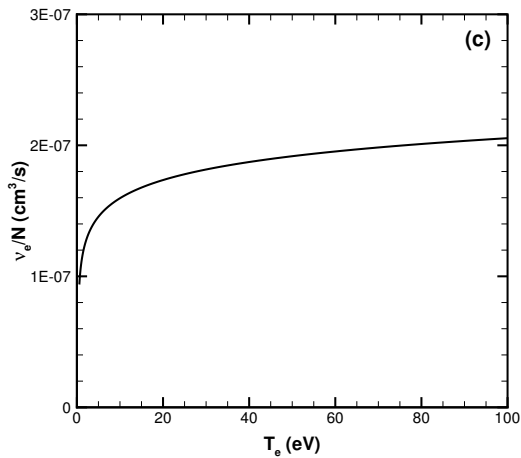


Figure 2. Test of Boltzmann solver: predicted Townsend ionization coefficient for nitrogen compared to experimental data of Haydon and Williams.³³



(b) Rates of vibrational excitation (Reactions 43-50).



(c) Electron-neutral collision rate.

Figure 1. Quantities determined from zero-dimensional solution of Boltzmann equation.

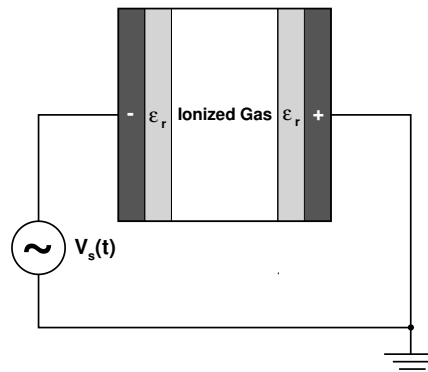
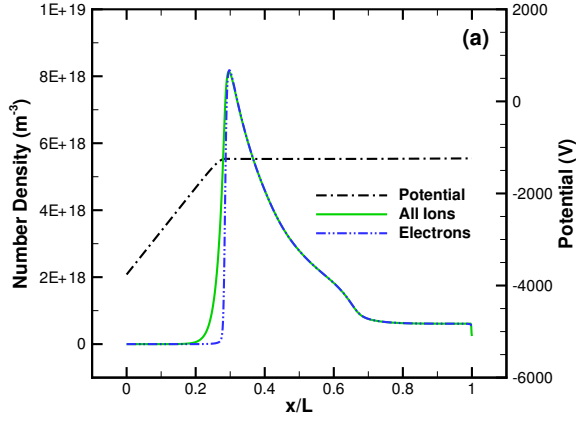
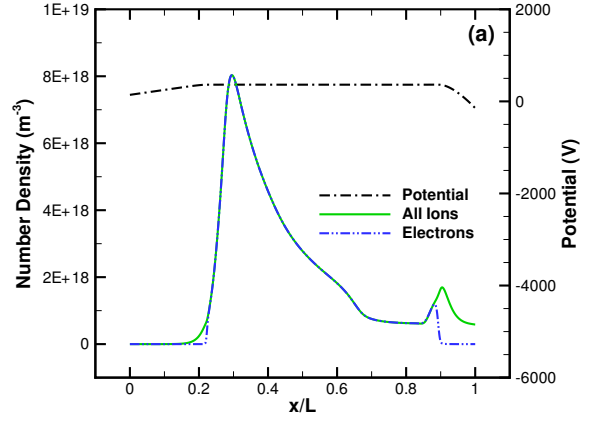


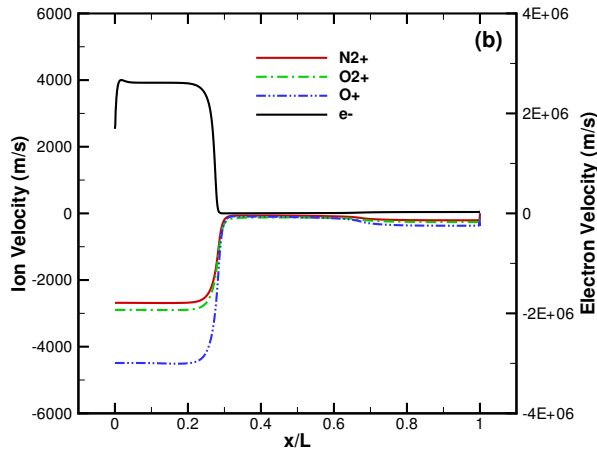
Figure 3. Diagram of computational domain.



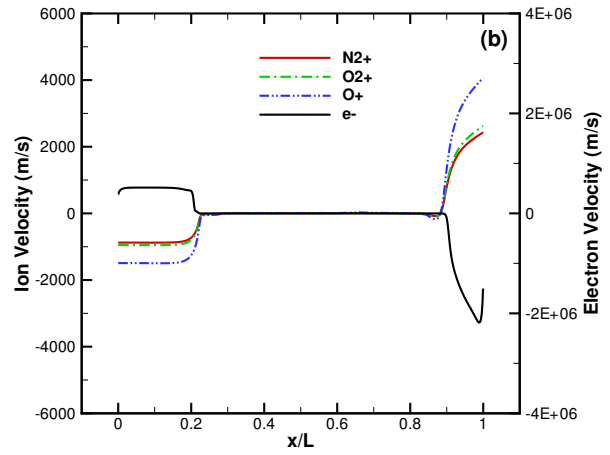
(a) Number densities and potential.



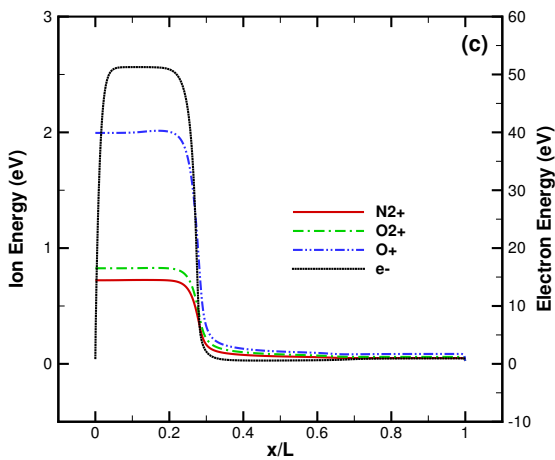
(a) Number densities and potential.



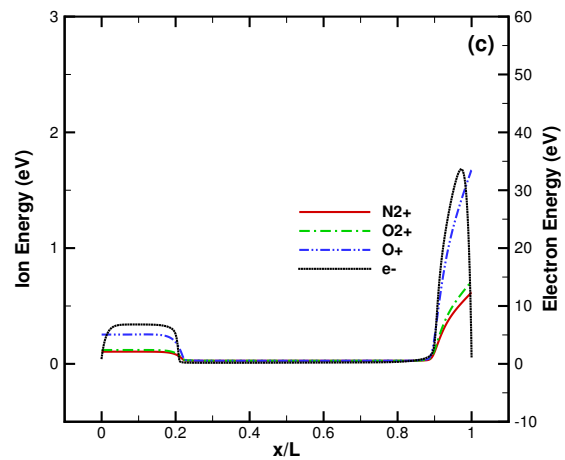
(b) Velocities.



(b) Velocities.



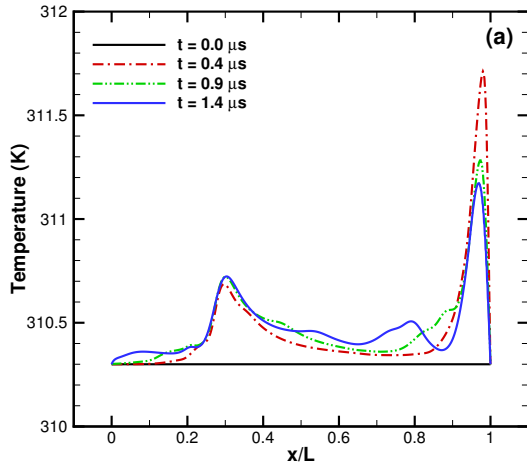
(c) Temperatures ($k_B T_s/e$).



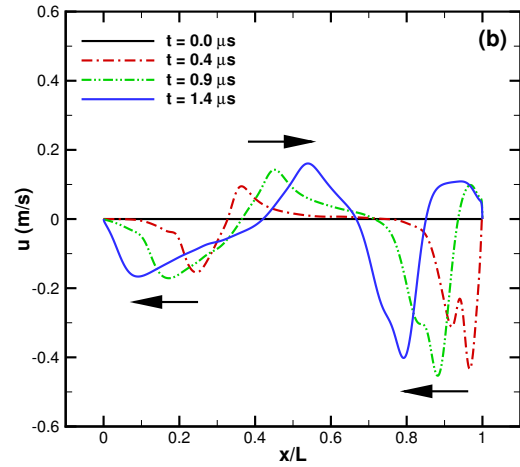
(c) Temperatures ($k_B T_s/e$).

Figure 4. Discharge profiles at 12 ns for $V_0 = 5$ kV.

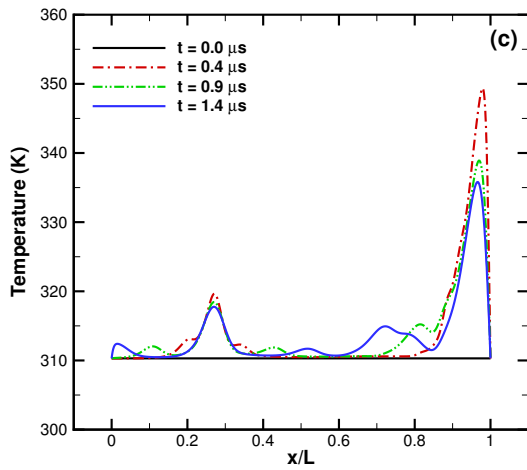
Figure 5. Discharge profiles at 24 ns for $V_0 = 5$ kV.



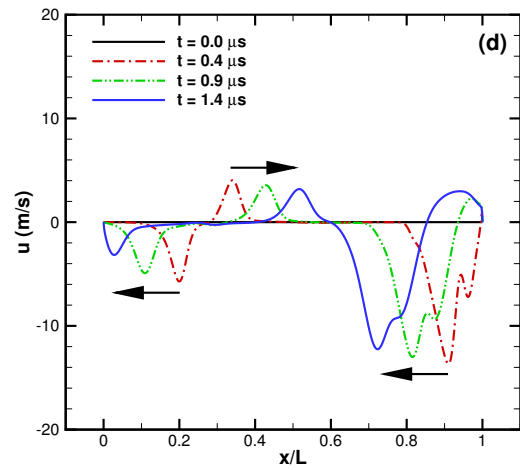
(a) Temperature, $V_0 = 5$ kV case.



(b) Velocity, $V_0 = 5$ kV case.



(c) Temperature, $V_0 = 27$ kV case.



(d) Velocity, $V_0 = 27$ kV case.

Figure 6. Profiles of the properties of the bulk gas for selected times in the simulation. Arrows indicate direction of wave motion.